Volume 13
Number 8
28 February 2025
Pages 2563–2880

Journal of Materials Chemistry B

Materials for biology and medicine

rsc.li/materials-b

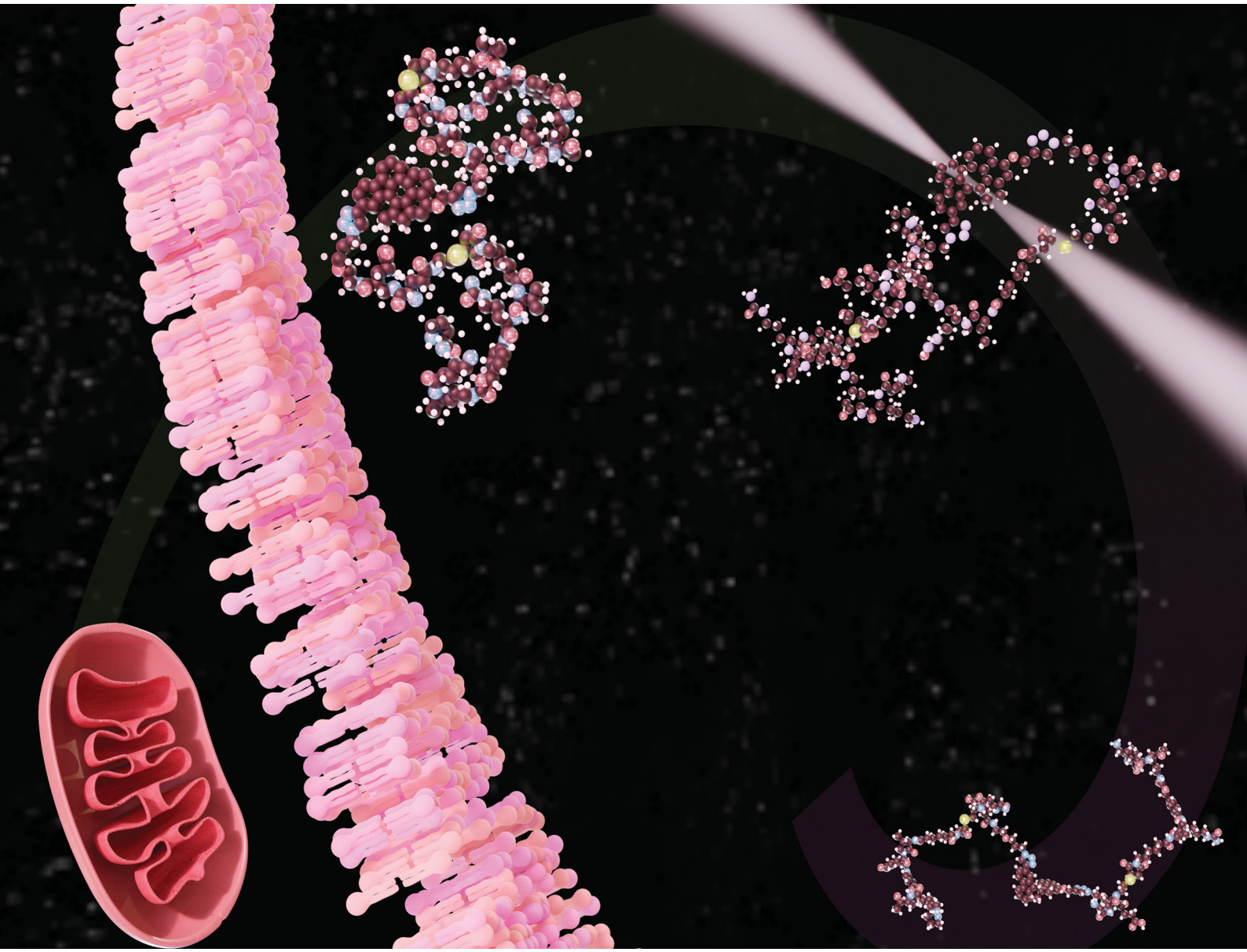

ISSN 2050-750X

ROYAL SOCIETY OF CHEMISTRY

COMMUNICATION

B. Feringa and M.J. Vicent Labs *et al.*
A light-driven molecular motor-polypeptide conjugate supports controlled cell uptake

Journal of Materials Chemistry B

ROYAL SOCIETY OF CHEMISTRY

COMMUNICATION

View Article Online
View Journal | View Issue

Check for updates

Cite this: *J. Mater. Chem. B*, 2025, **13**, 2658

Received 30th October 2024,
Accepted 9th December 2024

DOI: 10.1039/d4tb02434f

rsc.li/materials-b

A light-driven molecular motor-polypeptide conjugate supports controlled cell uptake†

Camilla Pegoraro, ‡[a] Ainoa Guinart,‡[b] Esther Masiá Sanchis, [acd] Daniel Doellerer, [b] Marc C. A. Stuart, [b] Inmaculada Conejos-Sánchez, *[ac] Ben L. Feringa *[b] and María J. Vicent *[acd]

While light-driven molecular motors (MMs) hold immense potential to control cell function, low biocompatibility and solubility have hampered their implementation. We developed a novel polypeptide-conjugated MM by linking a propargyl-derivatized light-driven MM to a poly-L-glutamic acid-based carrier (P) with inherent mitochondria tropism through click chemistry, denoted P-MM. P-MM effectively maintained the parental stability and unidirectional rotational capabilities of MM upon irradiation at 405 nm. Light-induced supramolecular conformational changes significantly increased cell uptake compared to non-irradiated controls while retaining the subcellular targeting capacity of P. P-MM exhibited minimal cytotoxicity and reactive oxygen species production, suggesting a non-disruptive interaction with cell membranes. Overall, we establish a connection between irradiation and enhanced biological responses, demonstrating the potential of integrating MMs with targeted polymeric nanocarriers for controlled, light-responsive behavior in biological systems and innovative applications in advanced therapeutic/diagnostic strategies.

Introduction

Light-based control of cell behavior offers advantages for manipulating biological systems, including rapid responses, high spatiotemporal resolution, non-invasiveness, and reversibility.[1] Incorporating photoswitches – molecules displaying reversible interconversions between conformational states upon light exposure – also supports control over cell function.[2,3] The emergence of rotary molecular motors (**MMs**) – derived from chiroptical molecular switches and based on overcrowded alkenes that support controlled molecular motion[4] – represented a significant advance due to their ability to perform repetitive, light-driven, and unidirectional rotations around a carbon–carbon double bond.[5] **MMs** meet the three fundamental criteria of a motorized machine: complete 360° unidirectional rotations, repetitive motions, and energy input from light;[6] however, low biocompatibility and solubility have limited their biological application.[7–9]

The development of **MMs** with chemical functionalities that allow further derivatization without altering motion may address these issues. Polypeptides offer biocompatibility, biodegradability, multivalency, and tunable design[10] and may enhance the biological/therapeutic applicability of **MM**. Polypeptides degrade into non-toxic metabolites, making them ideal for repeated administration without safety concerns.[11] Innovations in synthetic chemistry and polymerization techniques have significantly enhanced the precision and adaptability of polypeptide conjugation.[12] These advancements enable the integration of stimuli-responsive elements and the engineering of semitelechelic properties required for site-specific conjugation.[13] The precise control over the polypeptide structure ensures more efficient and targeted cargo delivery.

In this line, we attached an azide-derivatized poly-L-glutamic acid (PGA)-based carrier (**P**)[14,15] to a propargyl-derivatized light-driven **MM** to allow site-specific conjugation through click chemistry (**P-MM**). Apart from the semitelechelic properties in the polypeptide mainchain, **P** includes diblock oligomers of poly-L-ornithine (PLO) and polyproline (PLP) (PLO_n–PLP_m, $n:m$ ratio 1:3, referred to here as PP) as sidechains, conferring cytosolic delivery and mitochondrial targeting. We recently demonstrated the mitochondria tropism of **P** using a cardiolipin-specific interaction.[14,15] Conjugating PP to PGA preserved mitochondrial targeting abilities while enhancing safety by retaining cell uptake without compromising mitochondrial function or viability.[14,15]

Here, **P-MM** displayed stability and rotational cycling while undergoing conformational changes after irradiation at 405 nm,

[a] *Príncipe Felipe Research Center, Polymer Therapeutics Lab., 46012 Valencia, Spain. E-mail: iconejos@cipf.es, mjvicent@cipf.es*
[b] *Stratingh Institute for Chemistry, University of Groningen, Groningen 9747 AG, The Netherlands. E-mail: b.l.feringa@rug.nl*
[c] *Centro de Investigación Biomédica en Red en Cáncer (CIBERONC), Instituto de Salud Carlos III, Spain*
[d] *Príncipe Felipe Research Center, Screening Platform, 46012 Valencia, Spain*

† Electronic supplementary information (ESI) available. See DOI: https://doi.org/10.1039/d4tb02434f

‡ Authors with equal contributions.

which supported increased cell uptake compared to non-irradiated **P-MM** while maintaining mitochondrial tropism. Our findings demonstrate a correlation between light-induced conformational changes and biological outcomes, paving the way for novel applications of **P-MMs** in biological systems.

Experimental

The ESI† provides more details regarding **P**, **MM**, and **P-MM** synthesis, characterization and the materials employed.

Synthesis of the polypeptide-molecular motor conjugate (P-MM conjugate)

An oven-dried vial was charged with **MM** (1.2 mg, 2.8 μmol, 0.5 eq.) and **P** (40 mg, 5.6 μmol, 1.0 eq.) in a mixture of DMSO : H_2O (1 : 1). Sodium ascorbate (40 mg, 5.5 μmol, 5.0 eq.), copper sulfate pentahydrate (1.4 mg, 5.6 μmol, 1.0 eq., and ligand (R)-MonoPhos(R) (0.04 mg, 0.112 μmol, 0.02 eq.) were added to the mixture. The reaction mixture was stirred for three days at room temperature. After DMSO elimination using a rotavapor and freeze-drying, the product was purified by PD-10 desalting columns packed with Sephadex G-25 resin.

UV-vis spectroscopy

UV-vis spectroscopy was used to evaluate **MM** and **P-MM** isomerization and for thermodynamic studies using an Agilent 8453 UV-vis diode array system equipped with a quantum northwest peltier controller. Unless specified, irradiations were conducted using a built-in setup coupled to a light emitting diode (LED). Solutions were prepared and measured using a 10 mm quartz cuvette. The same procedure was used for UV-Vis controls on **P**.

^{1}H-NMR *in situ* irradiation studies

A 1 mM solution of **MM** in its stable form ($\mathbf{MM_{Stable}}$) was prepared in $CDCl_3$ and transferred into an NMR tube fitted with a glass optic fiber for *in situ* irradiation studies. The sample was placed in a varian unity plus 500 MHz NMR and cooled to −15 °C. ^{1}H NMR spectra were recorded before irradiation, while irradiating at 405 nm until the PSS was reached, and during the THI step until completion. See the ESI† for further details.

Fluorescence spectroscopy

Fluorescence spectroscopy was used to evaluate the CAC of **P-MM** with and without light irradiation (at 405 nm) using the Nile red assay following previously established procedures (see ESI† for details). Sample solutions were excited at 550 nm and emission was recorded from 590 to 750 nm using a JASCO FP6200 fluorometer.

Cryo-transmission electron microscopy

P-MM samples (2 mM) were placed on a glow-discharged holy carbon-coated grid (quantifoil 3.5/1, QUANTIFOIL Micro Tools GmbH). After blotting, the corresponding grid was rapidly frozen in liquid ethane (Vitrobot, FEI) and kept in liquid nitrogen until measurement. The grids were observed with a Gatan model 626 cryostage in a Tecnai T20 Field Electron and Ion Company (FEI) cryo-electron microscope operating at 200 keV. Cryo-TEM images were recorded on a slow-scan charge-coupled device (CCD) camera under low-dose conditions. All processes were performed in the dark. For irradiated samples (405 nm), the same procedure was carried out in a quartz cuvette immediately before freezing.

Circular dichroism

CD spectroscopy was performed using a J-815 CD Spectrometer (JASCO Corporation), incorporating a Peltier thermostated cell holder (PTC-423, JASCO Corporation) equipped with a recirculating cooler (JULABO F250, JASCO Corporation). A nitrogen flow of approximately 1.5 L min^{-1} was directed through the spectrometer and regulated using a nitrogen flow monitor (Afriso Euro-Index). Samples were prepared in PBS buffer and irradiated at 405 nm for 5 minutes. PP was used as a reference for a PPII profile. Each sample was analyzed three times (n = 3) in a quartz cuvette with a 1 mm diameter.

Cell viability assays

MDA-MB-231 cells were seeded in 96-well plates (5000 cells per well) and incubated for 24 h at 37 °C with 5% CO_2. **P** and **P-MM** were prepared as stock solutions in PBS buffer diluted in DMEM/F-12 medium (with 10% fetal bovine serum (FBS) and 1% penicillin/streptomycin (P/S)), sterilized, and added to cells at final concentrations of 0–1 mg ml^{-1}. Cell viability was assessed using the CellTiter-Glo® 2.0 assay after 24 or 72 h of incubation, with ATP luminescence measured using a CLARIOstar plate reader. For irradiation studies, cells were exposed to 405 nm UV light using a Lumidox® II LED system for 30 s, determined as the optimal non-toxic exposure time (see the ESI† for details) before or after **P-MM** treatment. Luminescence values were expressed as a percentage of cell viability relative to untreated controls, with results reported as mean ± SD (n = 3).

Internalization studies by high-throughput imaging in cell analyzer

Cellular uptake of **P** and **P-MM** (with and without 405 nm irradiation for 30 s) was analyzed using the high-throughput imaging HCS system IN cell analyzer 2200 with specific fluorescent markers (Invitrogen™ CellTracker™ Red CMTPX Dye (cytosol), Helix NP™ Green (nuclei), and Cy5 (**P-MM** and **P**)). MDA-MB-231 cells were seeded in 96-well plates and incubated for 24 h, followed by treatment with fluorescent markers and Cy5-labeled **P** or **P-MM**. After irradiation, fluorescence was measured every 20 min for 6 h. Data analysis involved normalizing fluorescence intensity to Cy5, accounting for quenching effects due to irradiation. Quenching conversion factors were determined (see the ESI† for details), and statistical significance was assessed using a t-test, with p-values indicating $p^{****} < 0.0001$; $p^{***} < 0.001$; $p^{**} < 0.01$; $p^{*} < 0.05$; ns: non-significant.

Internalization studies by confocal fluorescence microscopy

Cellular uptake of **P-MM** (with and without 405 nm irradiation) was qualitatively analyzed using confocal fluorescence microscopy with a Leica TCS SP8 confocal microscope. MDA-MB-231 cells were seeded in 384-well plates and incubated for 24 h. Pulse-chase studies were performed using MitoTracker™ Red (mitochondria), LysoTracker™ Green (lysosomes), and Cy5-labeled **P-MM** added at various time points (20, 40, 80, 120, 160, 200 min) and irradiated for 30 s when applicable. Control cells were used to establish autofluorescence levels. Image processing was carried out using Leica Application Suite X and Image J-JACoP for Pearson's correlation coefficient (Pearson *r*) calculation.

Reactive oxygen species production

MDA-MB-231 cells were seeded in 6-well plates and incubated for 24 h. Cy5-labeled **P** and **P-MM** were added and irradiated for 30 s at 405 nm. After 3 and 24 h, cells were washed, trypsinized, and resuspended in fresh medium. Cells were incubated with 2,7-dichlorodihydrofluorescein (DCFH) and propidium iodide (for viability assessment) and analyzed using flow cytometry. Data were collected with 10 000 counts per sample, analyzed using CytExpert software, and normalized to control levels. Control cells were used to determine autofluorescence. Statistical analysis was performed using a *t*-test, with significance levels set at $p^{***} < 0.0001$; $p^{***} < 0.001$; $p^{**} < 0.01$; $p^{*} < 0.05$; ns: non-significant. Values represent mean ± SD ($n = 3$).

Results and discussion

P-MM synthesis

The ESI† provides detailed reaction conditions and schemes for synthesizing **MM** functionalized with two click-chemistry handles for **P** attachment. We synthesized ketone **S1** from 1-methoxynaphthalene using a one-pot Friedel–Crafts acylation reaction followed by a Nazarov cyclization reaction.[16,17] We then deprotected **S1** with pyridine hydrochloride at elevated temperatures to yield phenol **S2**.[18] We reacted propargyl bromide protected with triisopropylsilyl chloride (**S3**)[18] with phenol **S2** in a Williamson-ether synthesis reaction to generate **S4**. We next converted the ketone moiety to a thioketone (generating **S5**) using Lawesson's reagent, completing the upper half of **MM**. We obtained the bottom half of **MM** (**S7**) by reacting the corresponding aryl halide (**S6**) with trimethylsilylacetylene using Sonogashira cross-coupling followed by transformation of **S7** into hydrazine, followed by manganese dioxide oxidation to form the respective diazo compound **S8**. We introduced the sterically overcrowded olefinic bond between both halves using Barton–Kellogg coupling between **S5** and **S8**, yielding **S9** at a 20% yield, which we further deprotected using tetra-*n*-butylammonium fluoride (TBAF) to obtain the final **MM**. Compound **MM** was isolated as a mixture of two isomers; attempts to separate the isomers by high-performance liquid chromatography (HPLC) failed due to low polarity.

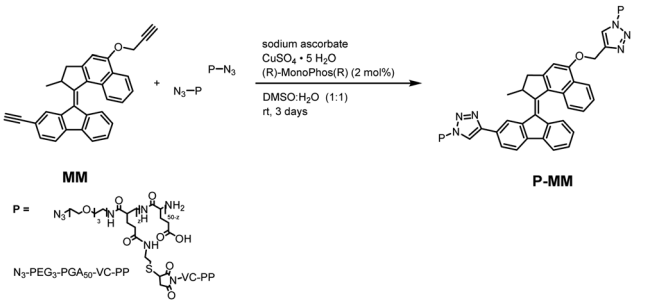

Scheme 1 Synthetic procedure for **P-MM**. rt: room temperature.

As previously detailed,[14,15] the preparation of **P** followed a convergent synthetic procedure (ESI,† Scheme S1). In brief, we functionalized (3.3 wt%) a linear semitelechelic PGA bearing a short azide-polyethylene glycol (PEG) chain (N_3-PEG_3-PGA_{50}) at the N-terminus through a valine–citrulline (VC) linker with a diblock copolymer (PLO_6–PLP_{22}, **PP**) by post-polymerization modification. The final negatively charged (−15.7 ± 0.2 mV) **P** displayed an average size of 5 nm (by SAXS), lacked toxicity at tested concentrations, but displayed energy-independent cell uptake and mitochondrial targeting.[14,15]

We obtained **P-MM** by reacting **MM** and **P** (1 : 2) in a mixture of DMSO : H_2O (1 : 1) *via* a copper-catalyzed click reaction with sodium ascorbate left to stir for three days at room temperature (Scheme 1 and Scheme S2, ESI†). Purification of **P-MM** using PD-10 desalting columns packed with Sephadex G-25 resin resulted in a yield of 90%. We evaluated **P-MM** synthesis by Raman spectroscopy *via* the disappearance of the alkyne peaks of **MM** (Fig. S1, ESI†) and by InfraRed spectroscopy *via* the disappearance of P's azide peaks (Fig. S2, ESI†) due to the masking effect of **P** on **MM** signals in the **P-MM** ^{1}H-NMR spectra (see ESI† for details). Together, these results confirm the successful synthesis and characterization of a novel polypeptide-conjugated molecular motor, which represents a significant advancement in the design of multifunctional biomolecular systems.

Analysis of the rotation cycle of P-MM

We investigated the photochemical/thermodynamic behavior of **P-MM** using steady-state spectroscopy and low-temperature ^{1}H-NMR. We confirmed the rotation cycle of **MM** using direct *in situ* irradiation of the NMR probe with a glass fiber optic cable connected to a 405 nm light-emitting diode at −15 °C in $CDCl_3$. Constant irradiation of the stable isomer decreased the peak intensity of corresponding protons (Fig. 1A-i), while new peaks emerged due to the **MM** metastable isomer (Fig. 1A-ii). The photostationary state (PSS) was reached when no changes in the proton spectra occurred under constant irradiation, with a stable-to-metastable isomer ratio of 40 : 60 (Fig. 1A-ii and Fig. S3A, ESI†). Removal of irradiation led to the complete recovery of the stable isomer (Fig. 1A-iii, -iv and Fig. S3B, ESI†).

We investigated the photochemical properties of **MM** and **P-MM** using UV-Vis absorption spectroscopy in toluene (**MM**) and phosphate buffer saline (PBS) (**P-MM** and **P**). All **MM**

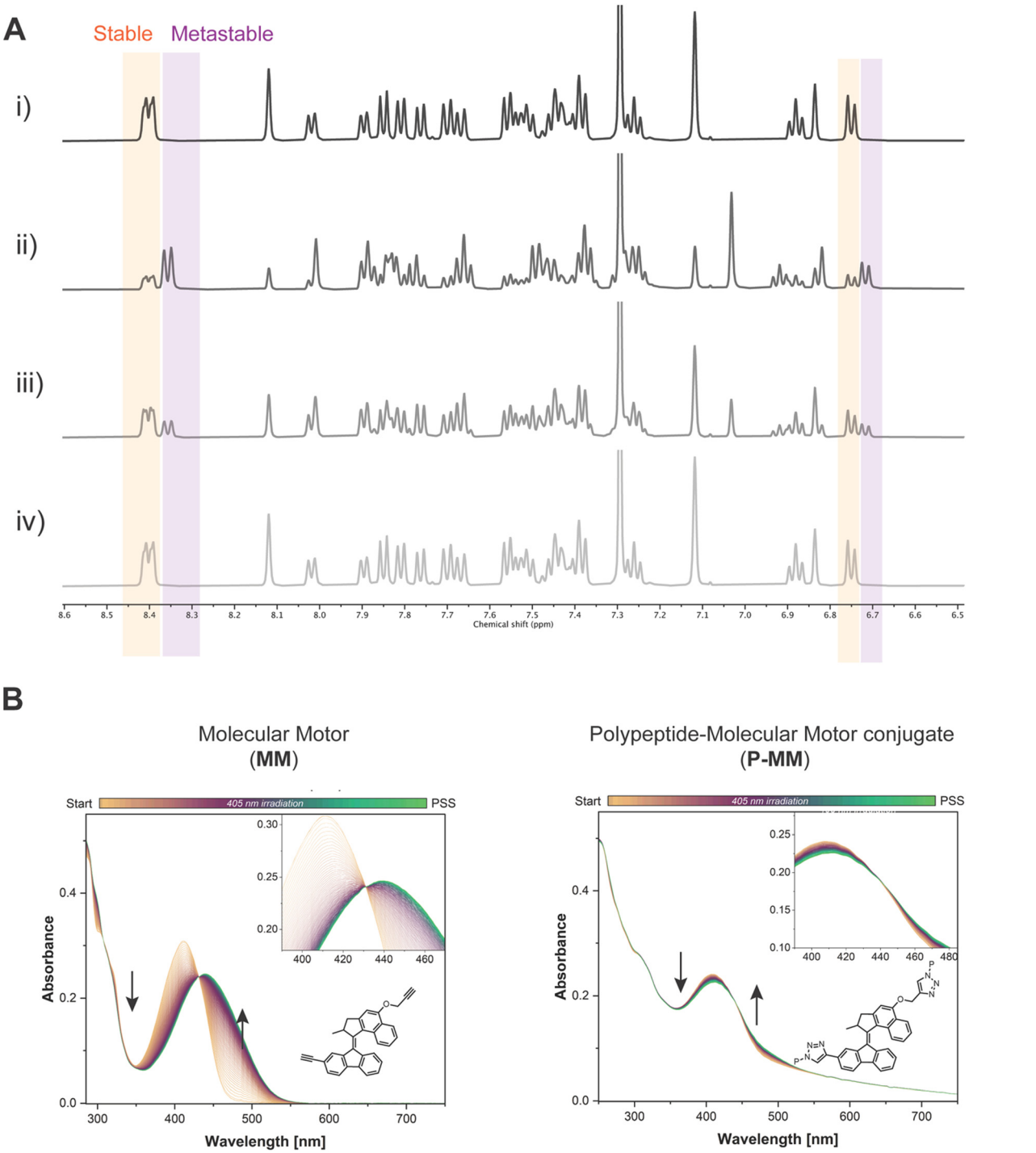

Fig. 1 Photochemical behavior of **MM** and **P-MM**. (A) ^{1}H-NMR aromatic peaks change **MM**. Starting from the stable isomer under dark conditions (i), irradiation at 405 nm until PSS (ii), turning off the irradiation, in the dark, partial thermohelix inversion (THI) (iii), in the dark, completed THI (iv). In $CDCl_3$, at −15 °C. (B) Changes to chemical structure and absorption spectra after 405 nm irradiation of **MM** (in toluene, 37 °C) and **P-MM** (in PBS, 37 °C). The inset shows the isosbestic point, with absorption changes indicated by the orange to green lines.

spectra displayed broad absorption bands with maxima centered ~410 nm, tailing further into the visible region (up to 555 nm) (Fig. 1B, orange line). The **MM** absorption exhibited a slight redshift compared to previous analogs,[19] likely due to the electron-donating effect of the oxygen atom in the upper half of **MM**, which is conjugated with the central double bond and the presence of alkyl groups. Irradiation of **MM** and **P-MM** at 405 nm at 37 °C changed the absorption spectra with a clear isosbestic point (Fig. 1B, insets).

The resulting steady-state spectra corresponded to the partial formation of metastable isomers at the PSS. We observed no change in the absorbance spectra of **P** when irradiated under the

same conditions (Fig. S4, ESI†). We next analyzed the thermodynamic parameters to determine the activation barriers of the thermal isomerization step (rotation cycle rate-determining process), which is the parameter defining rotational speed.[6] Eyring analysis was performed for **MM** and **P-MM** following the exponential decay at 450 nm of the absorbance in the absence of irradiation after reaching the PSS at various temperatures. Rate constants were obtained of the exponential decay function for each temperature and fitted using the linearized Eyring equation (Fig. S5, ESI†) to calculate the activation parameters of the thermal barrier. The calculated energy barriers for the metastable-to-stable transitions at 18.95 and 22.14 kcal mol for **MM** and **P-MM**, respectively (Table S1, ESI†). These values correspond to a half-life for rotation of 2 s for **MM** and 425 s for **P-MM** at 37 °C, with the significant increase attributed to a higher degree of strain in the system in accordance with observations by Foy *et al.* also showing a decreased rotational frequency for an **MM** linked to a polymer network.[20]

The investigation of the photochemical and thermodynamic behavior of **P-MM** revealed the successful rotation and stability of the molecular motor cycle and notable changes in the activation energy (rotation speed) of **P-MM** compared to parental **MM**. These findings suggest that polypeptide attachment introduces additional strain, significantly slowing the rotational cycle of the motor. These results highlight the impact of conjugation on the dynamic behavior of molecular motors, offering valuable insights for the design of hybrid systems with tunable photomechanical properties.

Supramolecular behavior of P-MM

Circular dichroism (CD) spectroscopy was employed to assess changes in the secondary structure of **P** (adopts a random coil structure in contrast to the polyproline II [PPII] helix conformation of PP) compared to **P-MM** before/after irradiation (405 nm, 5 min). CD spectra for **MM** and **P-MM** suggested random coil conformations (Fig. S6, ESI†), indicating that **MM** conjugation did not alter the secondary structure of **P**; however, we observed conformational alterations for **P-MM** in solution. We studied the self-assembly of **P-MM** in PBS by determining its critical aggregation concentration (CAC) using the Nile red fluorescence assay[21] (ESI†). We observed values of 59.4 and 25.9 μM for non-irradiated and irradiated **P-MM** (Fig. S7 and Table S2, ESI†), with differences in values indicative of light-induced changes in the supramolecular conformation of **P-MM**.

Next, we used cryo-transmission electron microscopy (cryo-TEM) before/after irradiation to characterize the nanoscopic arrangement of **P-MM** (Fig. S8 and S9, ESI†). Non-irradiated **P-MM** formed micelles (~2–3 nm in diameter) of smaller size than parental **P**, likely due to the conformational compactness afforded by the hydrophobic conjugated **MM**. Upon irradiation, the same **P-MM** solution exhibited long worm-like structures (~1 × 10 nm in length). These observations suggest that light irradiation of the conjugate induces a structural reorganization in **P-MM**, transitioning from a compact micellar form to an extended supramolecular architecture. This conformational shift reflects changes in the supramolecular interactions within the system, driven by the conformational change of **MM** under light exposure. The irradiation-induced conformational transition of **P-MM** may enhance cell uptake, consistent with studies demonstrating nanoparticle shape's influence on internalization.[22–24]

In short, light irradiation did not alter the secondary structure of the polypeptide; however, the substantial decrease in CAC following 405 nm irradiation in combination with the transformation observed in cryo-TEM images indicates a significant light-induced change in the supramolecular organization of **P-MM**. These findings suggest that integrating light-responsive polypeptide systems can support the manipulation of cellular functions in a highly controlled manner.

Exploring the feasibility of P-MM for biological applications

We evaluated potential biological applications of **P-MM** by focusing on cell uptake studies in a triple-negative breast cancer (TNBC) cell line (MDA-MB-231). Cell viability studies assessed by measuring ATP-dependent luminescence over 24/72 h confirmed that **P** and **P-MM** displayed no significant cytotoxicity (Fig. S10, ESI†), demonstrating the biocompatibility of **MM** when conjugated to **P**. We determined optimal non-toxic irradiation times by exposing cells to 405 nm irradiation for 30, 60, and 120 s without **P**/**P-MM** treatment; overall, 30 s of irradiation (65 mW per well) did not significantly affect cell viability (Table S3 and Fig. S11, ESI†). This optimization step established a reliable foundation for exploring the **P-MM** conjugate in biological applications. Cells incubated with **P-MM** and immediately irradiated for 30 s at 405 nm failed to show signs of induced cytotoxicity after 3/24 h, further validating the safety of **P-MM** (Fig. 2A).

After confirming safety, we assessed the ability of **P-MM** to enhance cellular uptake relative to non-irradiated **P-MM** and the parent polypeptide **P**. We evaluated the cell uptake of **P-MM** after irradiation using Cy5-labeled derivatives (Scheme S3 and Fig. S12, ESI†) and high-throughput imaging. We incubated cells with Cy5-labeled **P** and **P-MM**, exposed them to 30 s of 405 nm irradiation (comparing to non-irradiated controls; ESI†), and quantified fluorescence intensity after cell segmentation every 20 min for 6 h (Fig. S13, ESI†). The data analysis accounted for varying Cy5 labeling percentages in each treatment and the quenching effect caused by 405 nm irradiation (as detailed in the ESI†). Our results demonstrated a significantly higher average fluorescence intensity for irradiated compared to non-irradiated **P-MM** and both forms of **P**, indicating enhanced uptake of irradiated **P-MM** (Fig. 2B). These studies support a correlation between conformational changes and biological outcomes. Moreover, we observed a higher fluorescence intensity decay over time for **P-MM** compared to **P** using equivalent dye conditions (Fig. S14, ESI†), which we attributed to **MM**.[25] Photoisomerizing molecules function as effective Förster resonance energy transfer acceptors when close to molecular dyes, decreasing their radiative activity.[26] Quenching produced the highest fluorescence intensity at the initial timepoint (20 min), followed by a slight reduction (Fig. S14, ESI†). To confirm cell internalization and the unaltered

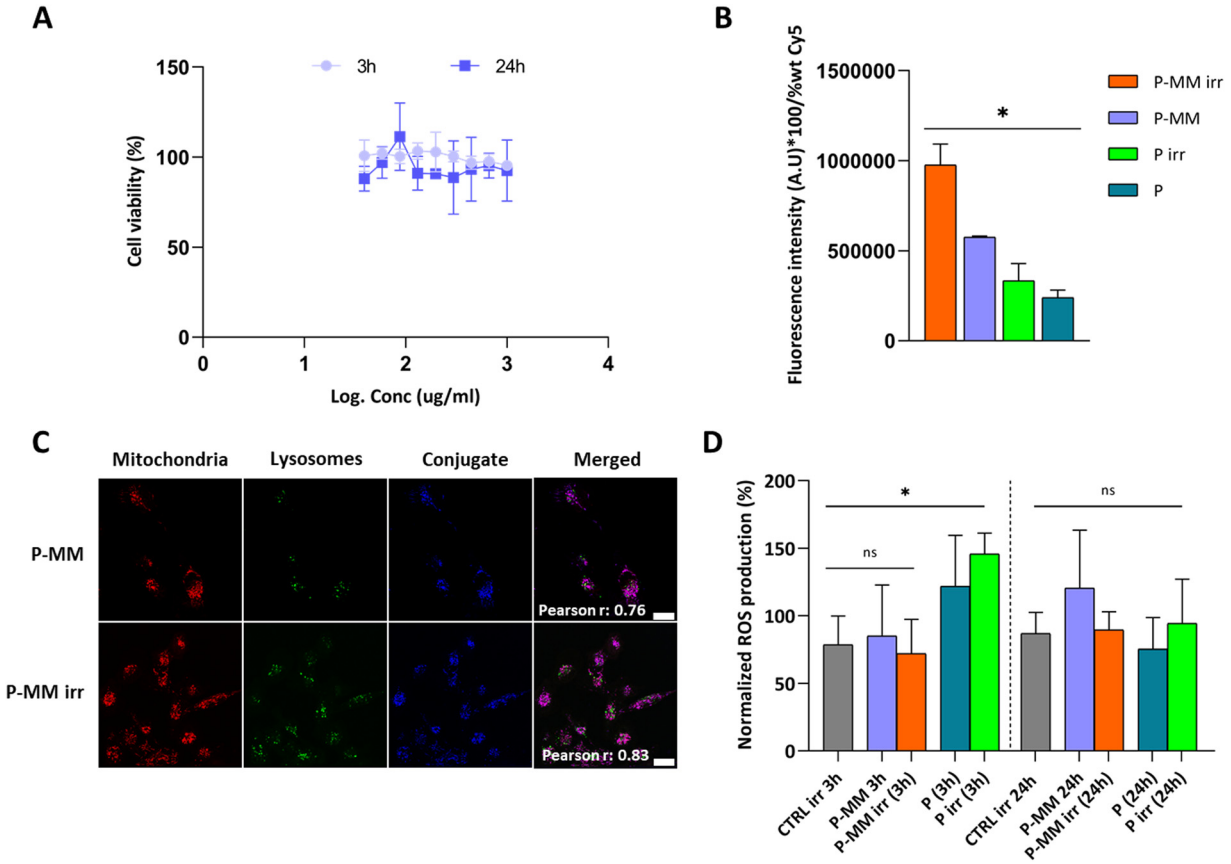

Fig. 2 Biological characterization of **P-MM**. (A) Cell viability after a 3-/24-h treatment and irradiation (405 nm, 30 s) with **P-MM** (n = 3, mean ± SEM). (B) Internalization of Cy5-labeled **P-MM** and **P** in irradiated (405 nm, 30 s) and non-irradiated conditions represented as the average fluorescence intensity measured after cell segmentation (CellTracker™ Red CMTPX Dye) in live cells (labeled with Helix NP™ Green) every 20 min over 6 h. Data normalized to wt% Cy5 (ESI†). t-Test comparing irradiated (irr) **P-MM** to **P**; n = 3, mean ± SEM; significance reported as $*p \leq 0.05$, ns = not significant. (C) Confocal images of **P-MM** uptake at 20 min post-treatment and irradiation (405 nm, 30 s) in cells following a pulse-chase experiment (Fig. S14, ESI†) (Red – MitoTracker™ Red CM-H2Xros for mitochondria; Green – LysoTracker® Green for lysosomes; Blue – Cy5 for **P-MM** and irradiated (irr) **P-MM**). Colocalization of **P-MM** and irradiated (irr) **P-MM** with Mitotracker red shown in the merge (purple). Pearson r (20 min) value calculated using the ImageJ – JACoP plugin. Scale bar: 10 μm. (D) Reactive oxygen species (ROS) levels after 3-/24-h treatment and irradiation (405 nm, 30 s) with **P** and **P-MM**. t-Test comparing to control set as 100% and treatments irradiated (irr) **P-MM**, **P-MM**, irradiated (irr) **P**, and **P** labeled with Cy5; n = 3, mean ± SEM. Significance reported as $*p \leq 0.05$, ns = not significant.

sub-organelle localization of **P** at the mitochondrial level[14,15] (even when conjugated to a molecular motor), we studied Cy5-labeled **P-MM** using live-cell confocal fluorescence microscopy before/after 30 s of 405 nm irradiation (pulse-chase study); we observed significant mitochondrial colocalization for **P-MM** after irradiation starting at 20 min (Pearson $r > 0.5$) (Fig. 2C) and remaining invariant over time (Fig. S15, ESI†). The stability of Pearson r values supports the hypothesis that light irradiation does not disrupt **P-MM**'s mitochondrial localization but rather facilitates consistent interaction with mitochondria.

To determine whether the mechanical rotation and conformational change associated with **P-MM** enhanced cell uptake, we assessed ROS generation after 3-/24-h treatment with Cy5-labeled **P-MM** and **P** with/without irradiation (30 s; 405 nm) to distinguish mechanical effects from oxidative stress induced by photosensitive systems.[27] Flow cytometry analyses revealed no significant increase in ROS levels for irradiated **P-MM** compared to control samples (Fig. 2D) at both time points; in contrast, treatment with **P** increased ROS levels at 3 h, suggesting a temporary oxidative stress response (followed by restoration of levels at 24 h).

Our results demonstrate that **P-MM** maintains a safe biological profile while significantly enhancing cellular uptake in MDA-MB-231 cells. The results suggest that increased uptake primarily derives from conformational changes induced by the mechanical rotation of **P-MM** rather than oxidative stress. These insights highlight the potential of **P-MM** for targeted delivery applications that require improved cell uptake and precise sub-organelle localization.

Conclusions

In conclusion, we report the synthesis and characterization of a light-driven rotary molecular machine bearing a polypeptide-conjugate with mitochondria tropism, which represents an

advance in designing multifunctional systems for biological applications. We determined that our synthetic molecular machine was suitable for click chemistry, offering numerous possibilities for biomolecular designs. **MM** conjugation did not alter P's inherent secondary structure and, therefore, mitochondrial tropism. We retained the rotation cycle of **MM**, with additional strain inducing a significant decrease in rotational speed. While the secondary structure of **P** remained unchanged, we observed significant irradiation-induced modifications in the supramolecular organization of **P-MM** – a transition from small micelles to elongated worm-like structures after irradiation. This conformational shift enhanced cell uptake compared to non-irradiated **P-MM** without a significant oxidative stress response. These findings suggest the potential of **P-MM** in acute intracellular applications, such as in targeted delivery systems and therapeutic strategies requiring improved cell uptake and precise sub-organelle localization. Future applications may include *ex vivo* lab-on-chip systems (benefit from precise control *via* an external trigger) and the acute systemic administration of biologically active agents (benefit from cytosolic transport).

Author contributions

C. P. and A. G. led the synthesis, data curation, formal analysis, investigation, methodology, and writing of the original draft. E. M. S., D. D., and M. C. A. S. contributed to the data curation, formal analysis, investigation, and methodology in supporting roles. Software development was equally contributed by C. P. and A. G. Cell viability assays and biological studies were carried out by C. P. with support from E. M. S. Supervision and project administration were equally managed by M. J. V. and B. L. F., supported by I. C.-S., C. P., A. G., I. C.-S., B. L. F. and M. J. V. contributed to the conceptualization and validation of the study. Funding acquisition was led by M. J. V. and B. L. F., with support from I. C. S. The manuscript was revised by C. P., A. G., I. C.-S., B. L. F. and M. J. V., with reviewing and editing contributions from all authors. All authors have read and approved the final version of the manuscript.

Data availability

The data supporting this article have been included as part of the ESI.† Further information if needed can be provided by the corresponding authors upon request.

Conflicts of interest

The authors declare a filed patent. M. J. Vicent; I. Conejos-Sánchez; C. Pegoraro; E. Karpova; G. Sogorb; C. Felip; V. J. Nebot; P. Schwille; Y. Qutbuddin. PCT/EP2024/068352 (Priority claimed: European Patent Application no. EP23382668.4). Polyproline-based Block-copolymers 28/06/2024. CIPF, PTS SL, and Max Planck Society.

Acknowledgements

This project was supported by the H2020-MSCA-ITN-2019 BIO-MOLMACS (proposal no. 859416). The authors acknowledge the Asociación Española contra el Cáncer (ICS INVES211323CONE Junior AECC grant), Spanish Ministry of Economy (PID2019-108806RB-I00), NextGeneration EU i + d + I funding through GVA Conselleria Innovació-Pol@Mets. Ref. MFA/2022/065 and European Regional Development Fund (PO FEDER Comunitat Valenciana 2014-2020) Generalitat Valenciana for financial support. Support from the project EU-OPENSCREEN IMPULSE (Grant Agreement No. 101132028), and the Netherlands Ministry of Education, Culture and Science (Gravitation Program no. 024.001.035) is gratefully acknowledged. We thank Dr Stuart P. Atkinson for his help in manuscript development and English editing, Alberto Hernandez for confocal imaging support, Alicia Martinez Romero for flow cytometry analysis, and Prof. Wesley Browne for Raman Spectroscopy.

Notes and references

1 C. Brieke, F. Rohrbach, A. Gottschalk, G. Mayer and A. Heckel, *Angew. Chem., Int. Ed.*, 2012, **51**, 8446–8476.
2 N. Vogt, *Nat. Methods*, 2020, **17**, 364.
3 W. A. Velema, W. Szymanski and B. L. Feringa, *J. Am. Chem. Soc.*, 2014, **136**, 2178–2191.
4 N. Koumura, R. W. J. Zijlstra, R. A. van Delden, N. Harada and B. L. Feringa, *Nature*, 1999, **401**, 152–155.
5 J. C. M. Kistemaker, A. S. Lubbe and B. L. Feringa, *Mater. Chem. Front.*, 2021, **5**, 2900–2906.
6 D. R. S. Pooler, A. S. Lubbe, S. Crespi and B. L. Feringa, *Chem. Sci.*, 2021, **12**, 14964–14986.
7 D. Liu, V. García-López, R. S. Gunasekera, L. Greer Nilewski, L. B. Alemany, A. Aliyan, T. Jin, G. Wang, J. M. Tour and R. Pal, *ACS Nano*, 2019, **13**, 6813–6823.
8 Q. Zhou, J. Chen, Y. Luan, P. A. Vainikka, S. Thallmair, S. J. Marrink, B. L. Feringa and P. van Rijn, *Sci. Adv.*, 2024, **6**, eaay2756.
9 A. Guinart, M. Korpidou, D. Doellerer, G. Pacella, M. C. A. Stuart, I. A. Dinu, G. Portale, C. Palivan and B. L. Feringa, *Proc. Natl. Acad. Sci. U. S. A.*, 2023, **120**, e2301279120.
10 T. Melnyk, S. Đorđević, I. Conejos-Sánchez and M. J. Vicent, *Adv. Drug Delivery Rev.*, 2020, **160**, 136–169.
11 A. Duro-Castano, I. Conejos-Sánchez and M. J. Vicent, *Polymers*, 2014, **6**, 515–551.
12 T. A. Bauer, L. Simić, J. F. R. Van Guyse, A. Duro-Castaño, V. J. Nebot and M. Barz, *Prog. Polym. Sci.*, 2024, **158**, 101889.
13 O. Zagorodko, J. J. Arroyo-Crespo, V. J. Nebot and M. J. Vicent, *Macromol. Biosci.*, 2017, **17**, 1–22.
14 C. Pegoraro, E. Karpova, Y. Qutbuddin, E. Masiá Sanchis, P. Dimitrijevs, C. Huck-Iriart, S. Gavrilović, P. Arsenyan, P. Schwille, C. Felip-León, A. Duro-Castaño, I. Conejos-Sánchez and M. J. Vicent, *Adv. Mater.*, 2024, DOI: **10.1002/adma.202411595**.
15 PCT/EP2024/068352, CIPF; PTS SL; and Max Planck Society, 2024.

16 F. K.-C. Leung, T. van den Enk, T. Kajitani, J. Chen, M. C. A. Stuart, J. Kuipers, T. Fukushima and B. L. Feringa, *J. Am. Chem. Soc.*, 2018, **140**, 17724–17733.
17 L. Pfeifer, M. Scherübl, M. Fellert, W. Danowski, J. Cheng, J. Pol and B. L. Feringa, *Chem. Sci.*, 2019, **10**, 8768–8773.
18 L. Pfeifer, N. V. Hoang, M. Scherübl, M. S. Pshenichnikov and B. L. Feringa, *Sci. Adv.*, 2024, **6**, eabb6165.
19 J. Vicario, A. Meetsma and B. L. Feringa, *Chem. Commun.*, 2005, 5910–5912.
20 J. T. Foy, Q. Li, A. Goujon, J.-R. Colard-Itté, G. Fuks, E. Moulin, O. Schiffmann, D. Dattler, D. P. Funeriu and N. Giuseppone, *Nat. Nanotechnol.*, 2017, **12**, 540–545.
21 M. C. A. Stuart, J. C. van de Pas and J. B. F. N. Engberts, *J. Phys. Org. Chem.*, 2005, **18**, 929–934.
22 B. Karagoz, L. Esser, H. T. Duong, J. S. Basuki, C. Boyer and T. P. Davis, *Polym. Chem.*, 2014, **5**, 350–355.
23 J. Zhao, H. Lu, S. Wong, M. Lu, P. Xiao and M. H. Stenzel, *Polym. Chem.*, 2017, **8**, 3317–3326.
24 S. Barua, J.-W. Yoo, P. Kolhar, A. Wakankar, Y. R. Gokarn and S. Mitragotri, *Proc. Natl. Acad. Sci. U. S. A.*, 2013, **110**, 3270–3275.
25 S. D. Pritzl, J. Morstein, S. Kahler, D. B. Konrad, D. Trauner and T. Lohmüller, *Langmuir*, 2022, **38**, 11941–11949.
26 A. Chevalier, P.-Y. Renard and A. Romieu, *Chem. – Asian J.*, 2017, **12**, 2008–2028.
27 J. L. Beckham, T. S. Bradford, C. Ayala-Orozco, A. L. Santos, D. Arnold, A. R. van Venrooy, V. García-López, R. Pal and J. M. Tour, *Adv. Mater.*, 2024, **36**, 2306669.